J. Solid Mech. 2026; 18(01): 15-34

Journal of Solid Mechanics

https://doi.org/10.57647/jsm.2026.1801.02

Research Article

A Comparative Assessment of DF2016 and MMC3 Fracture Criteria for Predicting Crack Initiation in Single Point Incremental Forming

Seyed Amin Teymouri Sendesi[1], Mohammad Mehdi Kasaei[1,2*], Majid Majidi[1], Seyed Jalal Hashemi[3]

[1]Department of Mechanical Engineering, Qa.C., Islamic Azad University, Qazvin, Iran
[2]Institute of Science and Innovation in Mechanical and Industrial Engineering (INEGI), Porto, Portugal
[3]Department of Mechanical Engineering, Technical and Vocational University (TVU), Tehran, Iran

***Corresponding author:** mm.kasaei@iau.ac.ir

Article History:

Received:
14 January 2026
Revised:
23 February 2026
Accepted:
23 February 2026
Published in Issue:
31 March 2026

Abstract

Accurately predicting fracture remains a significant challenge in single point incremental forming (SPIF) due to the complex and inherently nonlinear loading paths. This study presents a comparative evaluation of two advanced ductile fracture criteria, DF2016 and the modified Mohr-Coulomb (MMC3), for predicting crack initiation in SPIF of AA1050 aluminum sheets. The fracture models were calibrated using tensile tests and implemented in Abaqus/Explicit 2022 via a VUSDFLD user subroutine, coupled with a Swift-Voce hardening law. Numerical models were validated by comparing simulated thickness distributions and in-plane strains against experimental data from truncated conical and pyramidal specimens with variable wall angle. To account for the non-proportional loading characteristic of SPIF, a nonlinear damage accumulation rule, calibrated using the straight groove test, was incorporated to improve prediction precision. The results indicate that both criteria successfully predict the onset depth and location of cracks, demonstrating good agreement with experimental observations. However, the DF2016 criterion exhibited superior accuracy over MMC3, attributed to its enhanced capability to capture a wider range of deformation modes.

Keywords: Incremental forming, Fracture prediction, Crack depth, MMC3, DF2016 criterion

Cite this article: Teymouri Sendesi, S. A., Kasaei, M. M., Majidi, M., Hashemi, S. J., (2026). A Comparative Assessment of DF2016 and MMC3 Fracture Criteria for Predicting Crack Initiation in Single Point Incremental Forming, *Journal of Solid Mechanics,* 18(01): 15-34. https://doi.org/10.57647/jsm.2026.1801.02

1. Introduction

Incremental sheet forming (ISF) is a novel class of sheet forming processes that has attracted significant attention over the past few decades due to its efficiency in producing parts with complex geometries and its ability to reduce manufacturing costs [1]. Several processes, including traditional hammering and spinning, fall under the general category of incremental sheet forming. Specifically, ISF refers to a method in which a sheet is locally and incrementally deformed by the motion of a hemispherical tool until the desired final geometry is achieved. The sheet is clamped at the edges to prevent inward draw in, which leads to a noticeable reduction in wall thickness. Unlike the spinning process, in ISF the workpiece does not rotate, which allows independent control of the X, Y, and Z coordinates in the CNC machine and makes it possible to form asymmetric geometries.

This process is mainly used in rapid prototyping and customized production, where the cost of other forming methods may be prohibitively high [2]. The incremental sheet forming process can be performed without any additional support, known as single point incremental forming (SPIF) [3]. It can also be carried out with partial or full support, such as a die, in which case it is called two point incremental forming (TPIF) [4], or by employing a secondary independently controlled tool, referred to as dual sided incremental forming (DSIF) [5]. Ductile fractures are characterized by the material's ability to undergo plastic deformation and absorb energy before failure, and are specifically associated with the nucleation, growth, and coalescence of voids [6]. Fracture in incremental sheet forming, particularly in single point incremental forming, presents unique challenges due to the localized deformation and nonlinear strain paths. Jeswiet et al. [4] investigated asymmetric single point incremental forming of metal sheets and concluded that the small localized plastic deformation zone and the incremental nature of the ISF process significantly enhance formability, enabling the deformation of sheets with low inherent ductility. Emmens and Boogaard [7] examined the mechanisms that allow ISF to achieve strains beyond the forming limit curve (FLC) typical of conventional forming processes. A distinction was made between fractures and necking limit, and the role of localized deformation was emphasized as a critical factor in ISF. Jackson and Allwood [8] measured the strain distribution through the sheet thickness for both TPIF and SPIF processes. A comparison between the two methods showed that the deformation mechanisms in SPIF and TPIF involve stretching and shearing in a plane perpendicular to the tool path, with shear in the plane parallel to the tool direction being the dominant strain component. Babaei et al. [9] examined the effect of the single point incremental forming (SPIF) process on the mechanical and fracture properties of DC01 cold-rolled steel sheets. Fracture tests based on the essential work of fracture (EWF) method revealed notable increases in yield and ultimate tensile strengths but a significant drop in formability. Mechanical properties and fracture behavior also varied with the initial rolling direction. Scanning electron microscopy (SEM) analysis revealed ductile fracture as the dominant failure mode, with raw specimens showing higher essential work of fracture values. Sharma et al. [10] studied an experimental and numerical investigation of failure behavior in SPIF of AA6061-T6 sheets. Truncated cones and pyramid components with various wall angles were formed and analyzed through FE simulations and microscopic examination. Results showed that truncated cones exhibited higher formability than pyramids due to plane-strain deformation. Cracks initiated in the tool-sheet contact region and propagated due to bending and thinning effects. Overall, the study demonstrated that optimizing geometry and orientation can improve SPIF formability in low ductility alloys like AA6061-T6. Kumar et al. [11] investigated the failure mechanism in ISF of commercially pure aluminum alloy, AA1050. Experimental tests on truncated conical specimens revealed a sudden fracture when the wall angle increased from 71° to 72°. Finite element simulations with the GTN damage model supported these findings, showing similar stress evolution trends. Overall, the results demonstrate that inhomogeneous deformation and sudden increases in tensile hydrostatic stress are the primary causes of failure during ISF of AA1050. Gatea et al. [12] developed a modified damage model based on the Gurson-Tvergaard-Needleman (GTN) model, incorporating shear corrections to predict ductile fracture in the SPIF process through void nucleation and coalescence mechanisms. Their modified version demonstrated better accuracy than the original GTN model in predicting fracture under shear dominated loading conditions in SPIF. Mirnia and Shamsari [13] investigated ductile fracture in the SPIF process using the modified Mohr-Coulomb (MMC3) phenomenological model. Given the highly nonlinear loading path in SPIF, a nonlinear damage accumulation rule was employed to predict the onset of fracture. The comparison between predicted and experimental results for fracture depth and location showed good agreement, confirming the validity of using the MMC3 criterion in finite element (FE) simulations of SPIF. Wang et al. [14] evaluated the applicability of six damage models: Freudenthal, Cockcroft-Latham-Oh, Brozzo, Ayada, Rice-Tracey, and Lemaitre, for predicting fracture in the TPIF process. Their results revealed that the Ayada model provided the most accurate predictions for both the fracture depth and location. It was also observed that the occurrence in TPIF reduces the variation of stress triaxiality across the sheet thickness, which in turn influences damage accumulation. Bharti et al. [15] used the incremental sheet forming (ISF) process to fabricate three parts with different geometries and predicted fracture using non-coupled phenomenological damage models: Bao-Wierzbicki (BW), Hosford-Coulomb (HC), and modified Mohr-Coulomb (MMC). Their results showed that the Hosford-Coulomb model exhibited the best overall predictive capability among the investigated models within the applied loading range. Kumar and Tandon [16] investigated the incremental forming process based on the Lemaitre damage model. Conical parts were formed from AA1050-H14 aluminum sheets, and Scanning Electron Microscopy (SEM) was employed to identify the model parameters. Their findings revealed that shear, bending,

10.57647/jsm.2026.1801.02

and stretching are the dominant deformation modes in ISF, and the Lemaitre damage model can accurately simulate the process behavior. Kasaei et al. [17] investigated ductile fracture prediction in a newly developed hole-flanging joining process using five fracture criteria: McClintock, Rice-Tracey, Cockcroft-Latham, Brozzo, and modified Mohr-Coulomb (MMC). Among these, the MMC criterion predicted fracture at the outer edge of the flange with a negligible error of about 1%, and was recommended as the most suitable model for predicting fracture in this process. Lou et al. [18] proposed the DF2012 ductile fracture criterion to characterize the fracture behavior of DP780 steel sheets, emphasizing the mechanisms of void nucleation, growth, and coalescence during plastic deformation. This criterion was employed to construct fracture forming limit diagrams (FFLDs) and was validated against experimental results, particularly showing good performance under moderate stress triaxiality. The DF2012 model was also applied to Al 2024-T351 alloy and demonstrated strong agreement with experimental data under various stress conditions. In a subsequent study, Lou and Huh [19] extended this criterion to account for three dimensional stress states, including stress triaxiality and the Lode parameter. The model demonstrated high accuracy in predicting ductile fracture behavior. The transformed Mohr–Coulomb criterion also supported their findings, providing a reliable limit for stress triaxiality in ductile fracture. Lou et al. [20] later proposed an improved version, the DF2014 ductile fracture criterion, which introduced a variable cutoff value for the stress triaxiality value. This was achieved by redefining the triaxiality function from the DF2012 model. The new criterion successfully described ductile fracture behavior across a wide range of stress states, from biaxial compression to plane strain tension, and showed better agreement with experimental data for equivalent stresses and strains up to fracture compared with other criteria. Subsequently, Lou et al. [21] refined the DF2014 criterion by introducing DF2016 to simulate ductile fracture in AA6082-T6 alloy. The criterion was validated through tests including shear, uniaxial tension, plane strain tension, and balanced biaxial tension, demonstrating good predictive capability. Compared with MMC3, DF2012 and DF2014 criteria, the proposed criterion provides improved agreement with experiments and was recommended for predicting ductile fracture in metal forming processes. Behrens et al. [22] conducted experimental and numerical studies on the fracture behavior of high-strength steels using the modified Mohr–Coulomb, Johnson-Cook, and DF2016 criteria. In all simulations, fracture was predicted earlier than observed experimentally, and the accuracy of each model depended on the material type, with the JC model showing the largest deviation. Wang et al. [23] analyzed the fracture behavior of QP980 steel under various stress states: shear, uniaxial tension, and plane strain tension, using the DF2012 and four other ductile fracture models through combined experimental and numerical approaches. The comparison of force–displacement curves and fracture initiation points indicated that DF2012 yielded the lowest prediction error, which further improved after parameter optimization. Zeinali et al. [24] investigated fracture in a symmetric channel section during the roll forming of 6061-T6 aluminum sheets (2 mm thick) using the DF2012 criterion. Their results showed a 12.4% difference between simulated and experimental fracture locations, and it was found that increasing sheet thickness raised, while increasing bend radius reduced, the likelihood of fracture. Aksen et al. [25] used the DF2016 model to study anisotropic plasticity effects on ductile fracture and forming limit curves of DP600 and DP800 steels. Experimental tensile tests and finite element analyses were conducted using isotropic (von Mises) and anisotropic (HomPol6) yield criteria. Results showed that anisotropic calibration provides better agreement with experiments, emphasizing the importance of anisotropy in accurate fracture prediction for advanced high-strength steels. The ability to predict fracture contributes significantly to reducing production costs in forming processes through improved design and optimized process parameters. Given the proven predictive accuracy of the MMC3 criterion in incremental forming [13] and the enhanced capabilities of the newly developed DF2016 model [21], the present study investigates the effectiveness of these two ductile fracture criteria in capturing the onset of fracture in the single point incremental forming (SPIF) of AA1050 aluminum sheets. For this purpose, a series of experimental tensile tests including uniaxial tension (UT), in-plane shear (SH), plane strain tension (PS) and notched tension (NT), were conducted and subsequently simulated in Abaqus/Explicit 2022. The tension test simulation results were used to calibrate the models. To implement the fracture criteria in the simulations, the VUSDFLD subroutine was employed. Finally, the SPIF process of AA1050 alloy was simulated to predict the fracture initiation location and depth using these criteria. The simulation data were compared with experimental results, and the findings were analyzed and discussed.

2. Fracture criteria

Based on the microscopic analysis of ductile fracture and a comprehensive study of void nucleation, growth, and coalescence, Lou et al. [18] developed models to describe these processes. By combining them, they proposed a new ductile fracture criterion known as DF2012, expressed as Eq. 1:

$$\left(\frac{2\tau_{max}}{\bar{\sigma}}\right)^{C_1}\left(\frac{\langle 1+3\,\eta\rangle}{2}\right)^{C_2}\bar{\varepsilon}_f^p = C_3 \quad (1)$$

In this equation, the constants C_1, C_2 and C_3 are fracture parameters that must be calibrated using experimental data. Here, $\bar{\sigma}$ is the equivalent von Mises stress, τ_{max} denotes the maximum shear stress, η represents the stress triaxiality, and $\bar{\varepsilon}_f^p$ corresponds the equivalent plastic strain at fracture. In the principal stress space, the equivalent von Mises stress and the stress triaxiality are defined using Eqs. 2 and 3.

$$\bar{\sigma} = \sqrt{\frac{1}{2}[(\sigma_1-\sigma_2)^2+(\sigma_2-\sigma_3)^2+(\sigma_3-\sigma_1)^2]} \quad (2)$$

$$\eta = \frac{\sigma_m}{\bar{\sigma}} = \frac{\sigma_1+\sigma_2+\sigma_3}{3\bar{\sigma}} \quad (3)$$

Where σ_1, σ_2 and σ_3 denote principal stresses, ordered as $\sigma_1 \geq \sigma_2 \geq \sigma_3$, and σ_m is the hydrostatic (mean) stress. In this criterion, void nucleation is proportional to the equivalent plastic strain $\bar{\varepsilon}$, void growth is represented by the function $1+3\eta$ and void coalescence is expressed by the normalized maximum shear stress $(\frac{\tau_{max}}{\bar{\sigma}})$. Constants C_1 and C_2 control the different effects of nucleation, growth, and coalescence on ductile fracture, while C_3 corresponds to the equivalent plastic strain at fracture under uniaxial tension. The cutoff value of the stress triaxiality for this model is $\frac{-1}{3}$, below which fracture does not occur. Lou and Huh [19] extended the previous criterion into a model incorporating both stress triaxiality and the Lode parameter (L), by transforming the stress state from $(\sigma_1, \sigma_2, \sigma_3)$ to $(\eta, L, \bar{\sigma})$ as shown in Eq. 4.

$$\left(\frac{2}{\sqrt{L^2+3}}\right)^{C_1}\left(\frac{\langle 1+3\,\eta\rangle}{2}\right)^{C_2}\bar{\varepsilon}_f^p = C_3\,,$$

$$\langle \mathrm{x}\rangle = \begin{cases} \mathrm{x} & \text{when} \quad \mathrm{x} \geq 0 \\ 0 & \text{when} \quad \mathrm{x} < 0 \end{cases} \quad (4)$$

The Lode parameter is calculated according to Eq. 5.

$$L = \frac{2\sigma_2-\sigma_1-\sigma_3}{\sigma_1-\sigma_3} \quad (5)$$

The Lode parameter measures the influence of the second principal stress σ_2 and was initially proposed to assess its effect on yielding based on Tresca and von Mises criteria [26]. On the other hand, the stress state can be transformed from $(\eta, L, \bar{\sigma})$ to $(\sigma_1, \sigma_2, \sigma_3)$ as follows:

$$\sigma_1 = \sigma_m + s_1 = \sigma_m + \frac{(3-L)\bar{\sigma}}{3\sqrt{L^2+3}} = \left(\eta + \frac{(3-L)}{3\sqrt{L^2+3}}\right)\bar{\sigma} \quad (6)$$

$$\sigma_2 = \sigma_m + s_2 = \sigma_m + \frac{2\,L\bar{\sigma}}{3\sqrt{L^2+3}} = \left(\eta + \frac{2\,L}{3\sqrt{L^2+3}}\right)\bar{\sigma} \quad (7)$$

$$\sigma_3 = \sigma_m + s_3 = \sigma_m - \frac{(3+L)\bar{\sigma}}{3\sqrt{L^2+3}} = \left(\eta - \frac{(3+L)}{3\sqrt{L^2+3}}\right)\bar{\sigma} \quad (8)$$

Lou et al. [20] performed uniaxial compression and plane strain tests on AA5083-H32 and AZ31 alloys and concluded that the cutoff value for the stress triaxiality need not be constant $\frac{-1}{3}$, as it may depend on factors such as microstructure, deformation temperature, and strain rate. Therefore, the DF2012 criterion was modified to incorporate a variable cutoff value for the stress triaxiality, forming the DF2014 criterion as Eq. 9.

$$\left(\frac{2}{\sqrt{L^2+3}}\right)^{C_1}\left(\frac{f(\eta,L,C)}{f(\frac{1}{3},-1,C)}\right)^{C_2}\bar{\varepsilon}_f^p = C_3$$

$$f(\eta,L,C) = \eta + \frac{(3-L)}{3\sqrt{L^2+3}} + C \quad (9)$$

The parameter C, called the height of the cutoff value for the stress triaxiality, reflects the sensitivity of the triaxiality cutoff value to microstructural characteristics. When $C=0$, the triaxiality cutoff value corresponds to $\sigma_1 = 0$, $(-\frac{2}{3} \leq \eta \leq -\frac{1}{3})$, meaning the material does not fail under uniaxial, plane strain, or biaxial compression. For $C=\frac{1}{3}$, the cutoff value decreases by $\frac{1}{3}$ $(-1 \leq \eta \leq -\frac{2}{3})$, allowing fracture to occur under compressive states. The DF2014 criterion accurately describes fracture strains under shear, uniaxial tension, and plane strain tension. However, in sheet forming processes, four main loading conditions are important: shear, uniaxial tension, plane strain tension, and balanced biaxial tension [21]. To model fracture behavior under these four conditions, Lou et al. [21] modified the cutoff value for the stress triaxiality function as Eq. 10.

$$f(\eta,L,C) = \eta + C_4\frac{(3-L)}{3\sqrt{L^2+3}} + C \quad (10)$$

10.57647/jsm.2026.1801.02

In this modified cutoff value for the stress triaxiality expression, C_4 describes the influence of the Lode parameter, representing void distortion under Lode control and adjusting the dependence of the triaxiality cutoff value on the stress state. In numerical analyses, the DF2016 criterion is used in integral form as Eq. 11:

$$\frac{1}{C_3}\int_0^{\bar{\varepsilon}_f}\left(\frac{2}{\sqrt{L^2+3}}\right)^{C_1}\left(\frac{f(\eta,L,C)}{f\left(\frac{1}{3},-1,C\right)}\right)^{C_2} d\bar{\varepsilon} = D(\bar{\varepsilon}) \qquad (11)$$

Fracture begins when the accumulated damage parameter $D(\bar{\varepsilon})$ reaches a value of 1. Another criterion used in this study is the modified Mohr–Coulomb (MMC3) criterion. Bai and Wierzbicki [27] formulated the MMC3 model for linear loading paths, extending the stress-based Mohr–Coulomb model to three-dimensional space $(\bar{\varepsilon}_f^p, \eta, \bar{\theta})$ as follows:

$$\bar{\varepsilon}_f^p(\eta,\bar{\theta}) = \left\{\frac{K}{C_2}\left[C_3 + \frac{\sqrt{3}}{2-\sqrt{3}}(1-C_3)\right.\right.$$

$$\left.\left(sec\frac{\bar{\theta}\pi}{6}-1\right)\right] \qquad (12)$$

$$\left.\left[\sqrt{\frac{1+C_1^2}{3}}cos\frac{\bar{\theta}\pi}{6} + C_1\left(\eta+\frac{1}{3}sin\frac{\bar{\theta}\pi}{6}\right)\right]\right\}^{\frac{-1}{n}}$$

In Eq. 12, K, n, and $\bar{\theta}$ are the strength coefficient, strain-hardening exponent, and normalized Lode angle parameter, respectively. The normalized Lode angle is calculated as $\bar{\theta} = 1 - \frac{6\,\theta}{\pi}$, where the Lode angle θ is given by $\theta = \frac{1}{3}arccos\left(\frac{3\sqrt{3}J_3}{2J_2^{3/2}}\right)$. Here, J_2 and J_3 are the second and third deviatoric stress invariants. The relationship between the Lode parameter and Lode angle is expressed as: $L = \frac{(3tan\theta-\sqrt{3})}{(tan\theta+\sqrt{3})}$. The parameters C_1, C_2, and C_3 are material constants determined through calibration with experimental data.

3. Experimental tests

3.1. Preparation of calibration test specimens

Ductile fracture criteria require specific parameters that must be determined through experimental fracture tests. To accurately calibrate a ductile fracture criterion, it is essential to conduct tests that cover a wide range of stress states. For this purpose, sheet metal specimens with different geometries were cut along the rolling direction for various tests, including uniaxial tension (UT), in-plane shear (SH), plane strain tension (PS), and notched tension (NT) tests (Figure 1).

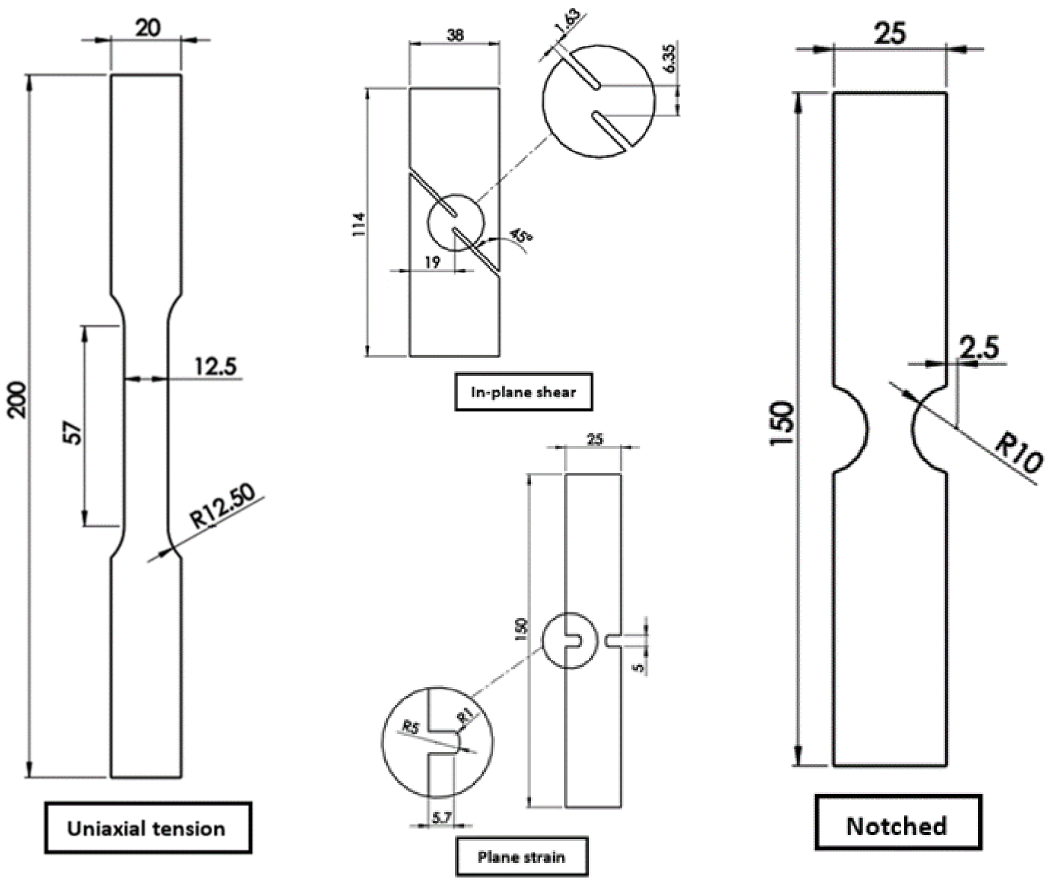

Figure 1. Dimensions of the specimens used in the tension

The specimens were cut using a laser cutting machine to ensure dimensional accuracy, and all of the tensile tests were conducted on a 40-ton SANTAM universal testing machine (Figure 2).

To ensure repeatability, three to five specimens were tested for each loading condition. An extensometer with a 50 mm gauge length was used to measure longitudinal strain. The test speed was set to 0.2 mm/min. The results of these tests were used to generate force–displacement curves, which were later employed to assess the accuracy of numerical simulations and to construct stress–strain curves for defining the plastic behavior of the material.

3.2. Preparation of SPIF specimens

To evaluate the performance of the DF2016 and MMC3 criteria, aluminum 1050 sheets with dimensions of 120×120 mm were formed using the single point incremental forming (SPIF) process. The SPIF formed parts included truncated pyramids and cones with variable wall angles and a depth of 30 mm (Figure 3). In addition, a straight-groove specimen was formed and simulated due to the simplicity of its geometry and the reduced computational time required, to calibrate the nonlinear damage model [13]. A circular grid with a 2.5 mm diameter was etched on the surface of each sheet to measure the in-plane major and minor strains. For this purpose, the sheet surface was first coated with black paint, and then the grid pattern was created using a laser. Tool paths were generated in PowerMILL software as 3D helical paths with a vertical step of 1 mm. The tool feed rate was set to 500 mm/min with no rotation. Mineral oil was used as a lubricant at the tool-sheet interface. Three specimens of each geometry were formed to ensure test repeatability. After forming, the locations and depths of cracks observed in the formed parts were compared with the corresponding predictions from the criteria in the simulations.

Figure 2. Tensile test specimen in the testing machine with extensometer

10.57647/jsm.2026.1801.02

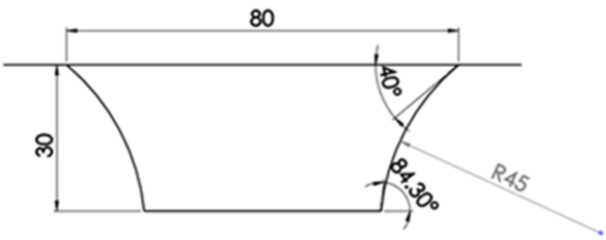

Figure 3. 2D schematic of the truncated conical and pyramidal specimens formed by the SPIF method

4. Simulation tests

4.1. Simulation of calibration tests

Finite element (FE) modeling of the tensile tests was performed using Abaqus/Explicit 2022. All tests were fully modeled using three-dimensional solid elements (C3D8R). The element size was determined based on the convergence of the fracture strain: 0.7 mm for the uniaxial tension, 0.4 mm for the plane strain, and notched tensile tests, and 0.25 mm for the in-plane shear test. In all tests, six elements were used through the sheet thickness in the critical region. Larger elements were used in non-critical regions to reduce computational cost. To minimize the simulation time, an explicit dynamic solver with a time scaling approach was employed, ensuring that the ratio of kinetic to internal energy remained negligible. The material was modeled as elastic–plastic material, and the plastic stress–strain data, extrapolated to higher strain values using the hardening law, were used to define the plastic behavior. Furthermore, the Hill 1948 yield criterion coefficients were implemented to represent the anisotropy of the sheet during plastic deformation. Field variables such as the damage index (D), stress triaxiality (η), and Lode parameter (L), along with the fracture criteria, were implemented in the software through the VUSDFLD subroutine.

4.2. Simulation of SPIF specimens

By simulating the incremental sheet forming (SPIF) process in Abaqus/Explicit 2022, the results were analyzed to assess the predictive performance of the DF2016 and MMC3 fracture criteria. The forming tool and the backing plate of the conical part were modeled as analytical rigid surfaces, while the pyramidal and straight-groove specimens were modeled without a backing plate; the sheets were constrained through boundary conditions instead. The S4R shell element, with an element size of 0.5 mm, was selected to model the sheet due to its ability to capture the stress state in ISF, accurately predict thickness variation under large deformations, and significantly reduce computational cost compared to solid elements [13, 14]. The element size was determined through mesh convergence analysis, and the edges of the sheet were fully constrained. The ductile fracture criteria, similar to other field variables, were implemented in Abaqus using the VUSDFLD subroutine. Crack initiation was modeled through the element deletion technique when the damage variable reached a value of 1. Because of the lubrication between the tool and the sheet, a low friction coefficient of 0.1 was assumed in accordance with Coulomb's law [28, 29].
The tool path coordinates in the X, Y, and Z directions were obtained from G-codes generated by PowerMILL and imported into Excel to determine the forming time corresponding to the tool positions.
Finally, both the time and the tool path coordinates were defined in Abaqus to simulate the forming process accurately.

5. Material behavior determination

To obtain the elastic-plastic behavior of the material, a dogbone specimen was fabricated according to the ASTM E 8M-04 standard and tested under uniaxial tension. After obtaining the force-displacement curve, the true stress-strain curve of the material was derived and used to define the elastic-plastic behavior in the simulation software. For strain levels beyond the necking point, an appropriate hardening law was applied.
To determine the anisotropy coefficients, the plastic strain ratio (also known as the Lankford coefficient or r-value) was used.
These coefficients are defined as the ratio of the width strain to the thickness strain in the uniaxial tensile test. Their use is considered essential for predicting material behavior during forming processes.
To determine the r-values, dogbone specimens were tested in uniaxial tension up to a strain level below the onset of necking (about 80%) in three orientations relative to the rolling direction: 0° (RD), 45° (DD), and 90° (TD). After testing, the true longitudinal strain ε_l along the loading direction and the true width strain ε_w perpendicular to it were measured.
Assuming plastic incompressibility ($\varepsilon_l + \varepsilon_w + \varepsilon_t = 0$), the thickness strain is obtained from Eq. 13:

$$\varepsilon_t = -\varepsilon_l - \varepsilon_w \tag{13}$$

After determining the width and thickness strains, the r-value can be calculated using Eq. 14:

$$r = \frac{\varepsilon_w}{\varepsilon_t} \tag{14}$$

Once the r-values were determined, the anisotropy parameters were calculated using Eqs. 15:

$$R_{11} = R_{13} = R_{23} = 1$$

$$R_{22} = \sqrt{\frac{r_{90}(r_0 + 1)}{r_0(r_{90} + 1)}}$$

$$R_{33} = \sqrt{\frac{r_{90}(r_0 + 1)}{r_0 + r_{90}}} \tag{15}$$

$$R_{12} = \sqrt{\frac{3r_{90}(r_0 + 1)}{(2r_{45} + 1)(r_{90} + r_0)}}$$

To describe the anisotropic behavior of the sheet in Abaqus, the Hill 1948 yield criterion was employed, which is widely used in sheet forming simulations due to its simplicity and accuracy. The coefficients of this criterion were calculated using the anisotropy parameters based on Eqs. 16:

$$F = \frac{1}{2}\left(\frac{1}{R_{22}^2} + \frac{1}{R_{23}^2} - \frac{1}{R_{11}^2}\right)$$

$$G = \frac{1}{2}\left(\frac{1}{R_{11}^2} + \frac{1}{R_{33}^2} - \frac{1}{R_{22}^2}\right)$$

$$H = \frac{1}{2}\left(\frac{1}{R_{11}^2} + \frac{1}{R_{22}^2} - \frac{1}{R_{33}^2}\right) \tag{16}$$

$$L = \frac{3}{2R_{23}^2}, \quad M = \frac{3}{2R_{13}^2}, \quad N = \frac{3}{2R_{12}^2}$$

The obtained coefficients are presented in Table 1.

Table 1. Lankford coefficient and Hill 1948 parameters

Lankford coefficient, r			Hill 1948 parameters					
0°	45°	90°	F	G	H	N	L	M
0.56	1.06	0.85	0.42	0.64	0.36	1.66	1.5	1.5

The true stress-strain curve obtained from the uniaxial tensile test was used to characterize the material's strain hardening behavior at large strains. Based on the experimental true stress-strain curve of the AA1050 alloy up to the onset of necking, the plastic behavior beyond this point was extrapolated using the combined Swift-Voce hardening law, as expressed in Eq. 17:

$$\sigma = \lambda\left[K(\varepsilon_0 + \varepsilon_p)^n + (1 - \lambda)[A + B(1 - e^{-c\varepsilon_p})]\right] \tag{17}$$

In this combined hardening law, K is the strength coefficient, n is the hardening exponent in Swift's law, A, B, and C are the parameters of Voce's law, ε_0 is the pre-strain, and λ is the weighting factor.

These parameters were first obtained by fitting the individual Swift and Voce models to the experimental true stress-plastic strain data up to the onset of necking.

To determine the weighting factor λ, the combined Swift-Voce model was refitted to experimental true stress-plastic strain data up to necking point (Figure 4). The parameters obtained from fitting the combined Swift-Voce hardening law to the true stress-plastic strain curve are presented in Table 2. The Swift-Voce hardening law was calibrated with a high fitting accuracy, as indicated by a coefficient of determination (R^2) of 0.992, confirming the reliability of the material parameters for numerical simulations.

Table 2. the calibrated parameters of the strain hardening law

K	n	λ	ε_0	A	B	c
181	0.037	0.46	8e-6	127.4	24	623.6

After determining the anisotropy coefficients and calibrating the combined Swift-Voce hardening law, the simulated force-displacement curve from the uniaxial tensile test was compared with the experimental one (Figure 5). The good agreement between these curves confirms the accuracy of the calibrated hardening law and the obtained anisotropy parameters.

6. Calibration of fracture criteria

To calibrate the fracture criteria, in addition to the uniaxial tension test, three other tests, in-plane shear tension, plane strain tension, and notched tension, were performed to capture various stress states. The presence of the four critical loading conditions in sheet metal forming, namely uniaxial tension, shear, plane strain, and balanced biaxial tension [21], justifies the calibration of both criteria using the aforementioned tensile tests.

All tensile tests were simulated in Abaqus/Explicit 2022 up to the fracture displacement obtained from the experimental tests. For the validation of the numerical simulations, the force-displacement curves obtained from the simulated tests were compared with those from the experimental tests.

The good agreement between these curves confirms the accuracy of the modeling and the reliability of the obtained results (Figure 6).

In the next step, the maximum equivalent plastic strain was assumed to represent the fracture strain. The element with the highest equivalent strain plays a critical role in evaluating material failure, as it corresponds to the region experiencing the most severe deformation and critical conditions.

10.57647/jsm.2026.1801.02

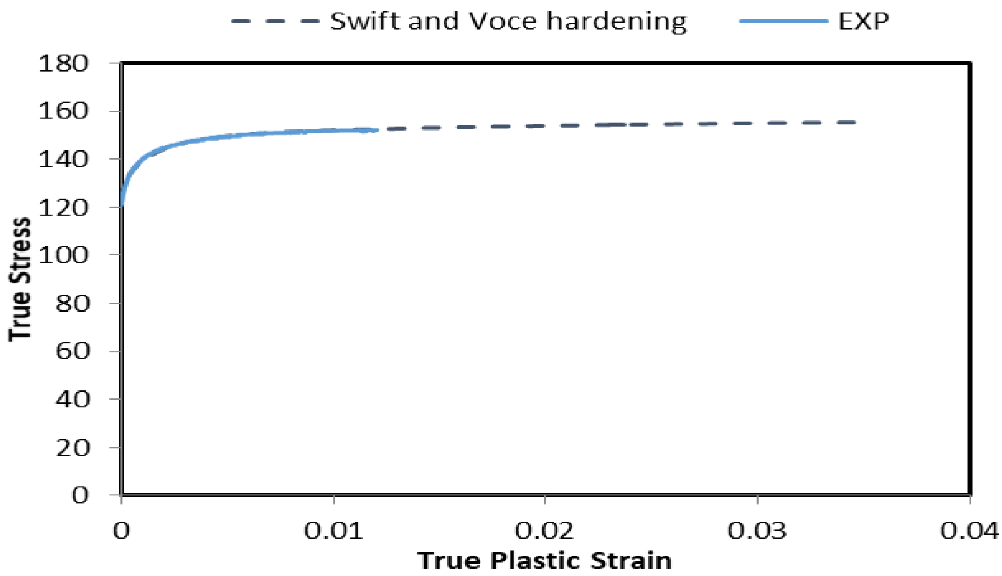

Figure 4. True stress- plastic strain curves from the experimental test and the calibrated Swift-Voce hardening law

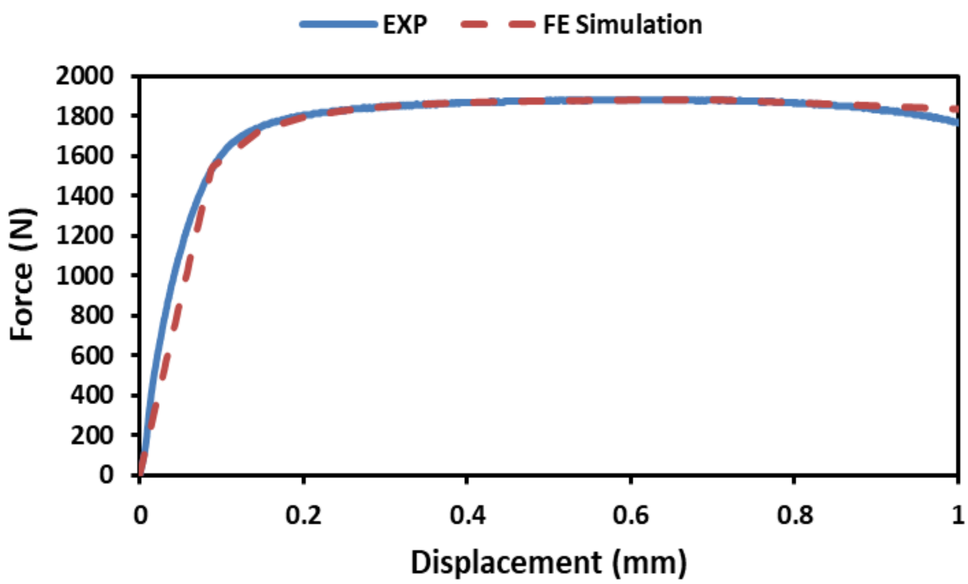

Figure 5. Force–displacement curves from the uniaxial tensile test, including experimental results and numerical predictions obtained using the Swift–Voce hardening law

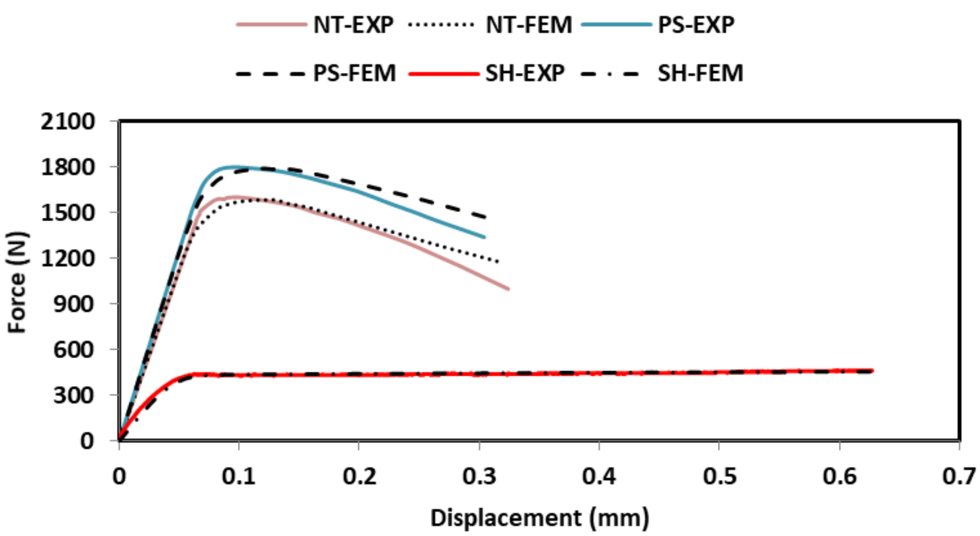

Figure 6. Evaluation of the force–displacement responses from experimental and simulated tensile tests

Evaluating the Lode parameter (L) and stress triaxiality (η) in this element helps ensure accurate prediction of fracture initiation and progression, and verifies that the material model and fracture criteria correctly reflect the actual material behavior under critical conditions. The stress triaxiality η and the Lode parameter L as functions of the equivalent plastic strain in the element with the highest equivalent strain for the tensile tests are presented in Figure 7. The evolution of the Lode parameter and stress triaxiality shows that they vary with increasing equivalent plastic strain. Therefore, their average values were used as calibration points to assess the modeled tensile tests, as defined by Eqs. 18 and 19.

$$\bar{\eta} = \frac{1}{\bar{\varepsilon}_f}\int_0^{\bar{\varepsilon}_f} \eta(\bar{\varepsilon})d\bar{\varepsilon} \qquad (18)$$

$$\bar{L} = \frac{1}{\bar{\varepsilon}_f}\int_0^{\bar{\varepsilon}_f} L(\bar{\varepsilon})d\bar{\varepsilon} \qquad (19)$$

The average values of stress triaxiality and Lode parameter, along with fracture strain obtained from simulations of different tensile tests used as calibration points, listed in Table 3.

Table 3. Average stress triaxiality and Lode parameter with fracture strain

Formability test	$\bar{\varepsilon}_f$	$\bar{\eta}$	$\bar{L}$
UT	0.22	0.41	-0.73
ST	0.30	0.054	-0.12
PS	0.13	0.59	-0.12
NT	0.136	0.55	-0.31

The average stress states of the tensile tests in the stress triaxiality-Lode parameter space are shown in Figure 8. As seen, the obtained results exhibit good agreement with plane stress conditions, confirming the reliability of the simulation and the validity of the average stress states used for criterion calibration.

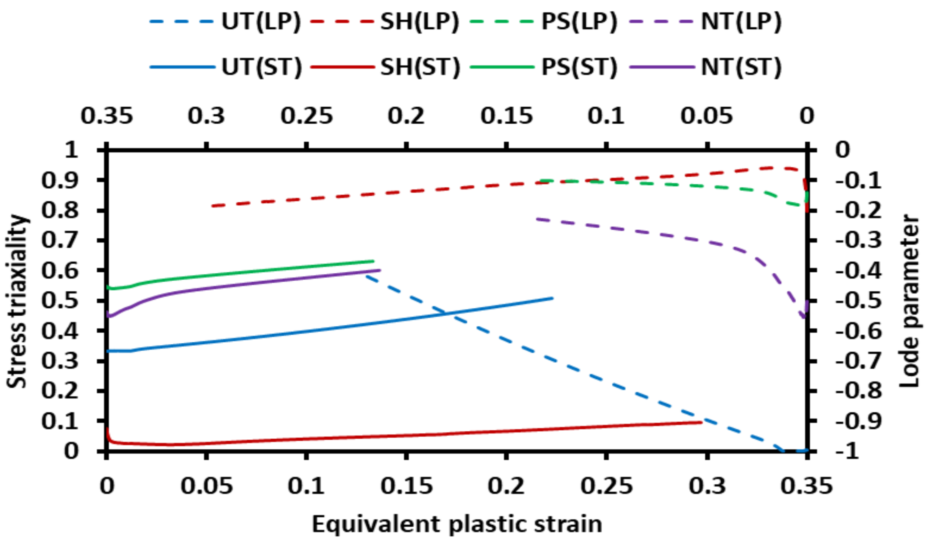

Figure 7. Evolution of stress triaxiality (ST) and lode parameter (LP) with increasing ε ̅^p for the tensile tests

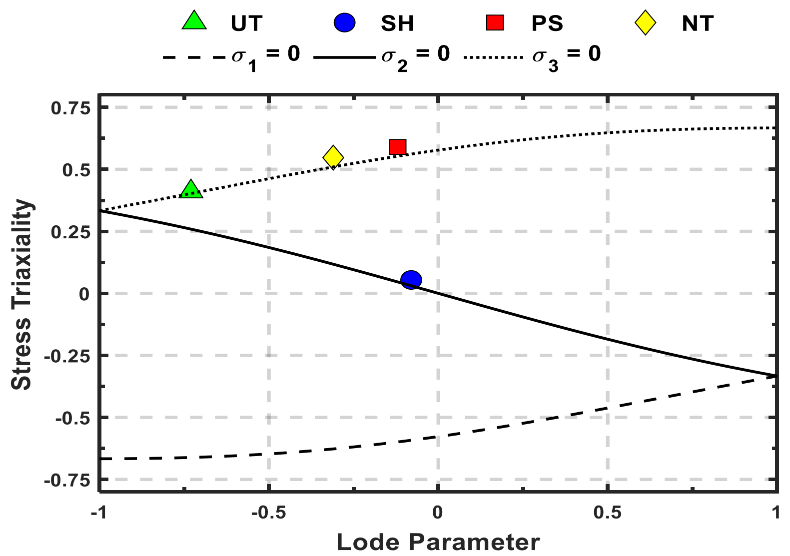

Figure 8. Average stress states in the tensile tests along with the plane stress conditions lines

To calibrate the criteria and determine the material constants, the 3D fracture loci of the MMC3 and DF2016 criteria were fitted to the calibration points using the Surface Toolbox in MATLAB, as shown in Figure 9. As can be seen, the fitted surfaces exhibit good agreement with the calibration points. With increasing stress triaxiality, void growth accelerates and the fracture strain decreases; conversely, as triaxiality decreases, the fracture strain increases. Negative values of stress triaxiality correspond to a compressive stress state, in which void growth is suppressed, resulting in a significant increase in fracture strain.

The three branches of plane stress, $\sigma_1 = 0, \sigma_2 = 0$ and $\sigma_3 = 0$, are shown on the fracture loci. These branches are obtained by setting Eqs. 6-8 equal to zero.

The material constants obtained from the calibration of the criteria are presented in Table 4.

Table 4. Obtained constants for the used criteria

Criterion	C_1	C_2	C_3	C_4	C
MMC3	0.034	89.7	0.894		
DF2016	6.27	3.35	0.355	2.55	0.33

The good agreement between the calibration points and the three branches of the plane stress conditions in the space of stress triaxiality and equivalent plastic strain is illustrated in the 2D fracture envelopes shown in Figure 10. Both models exhibit strong agreement with the calibration points in the tensile stress state, where the predicted fracture strains are nearly identical. However, the MMC3 criterion produces slightly lower fracture strain values than the DF2016 criterion. In the compressive region, the DF2016 model predicts higher fracture strains compared to MMC3. Consequently, the MMC3 model provides a more conservative estimate of fracture and is expected to predict an earlier onset of failure.

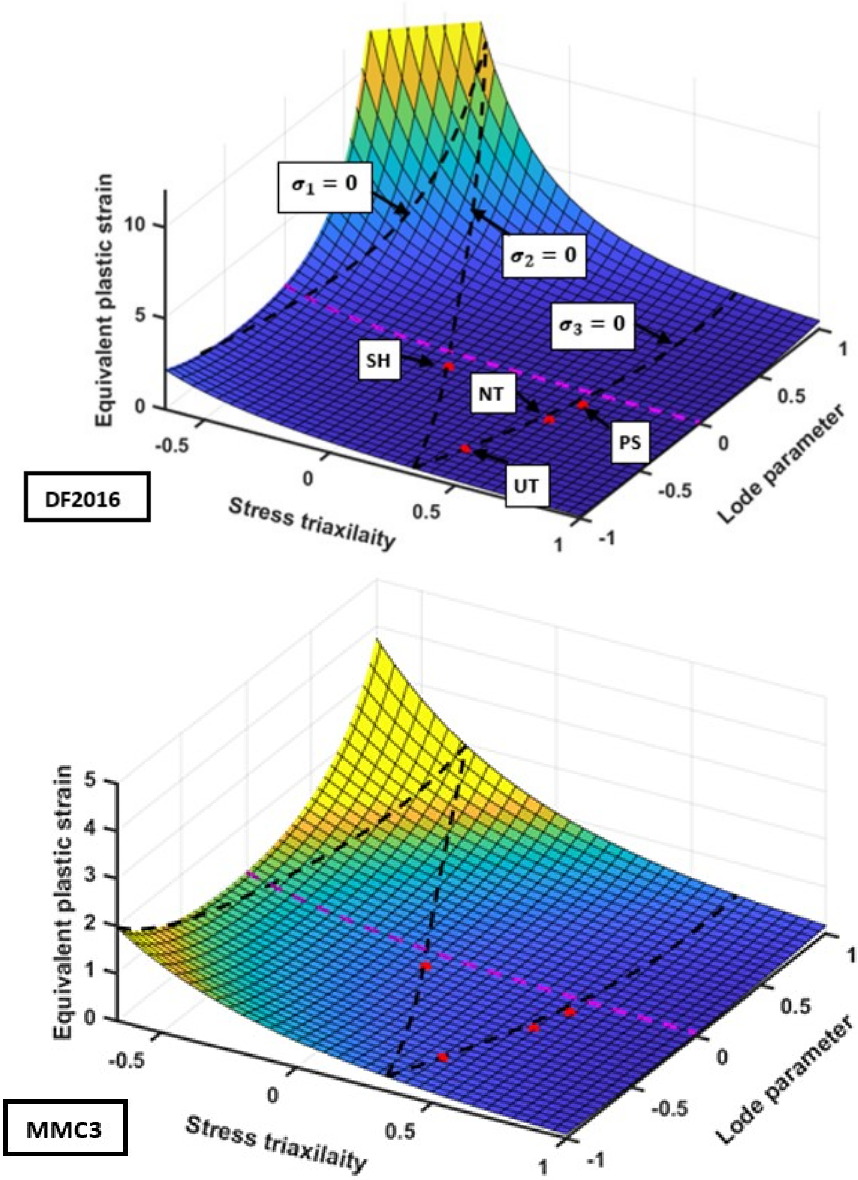

Figure 9. Fracture loci of AA1050 constructed by DF2016 and MMC3 criteria

10.57647/jsm.2026.1801.02

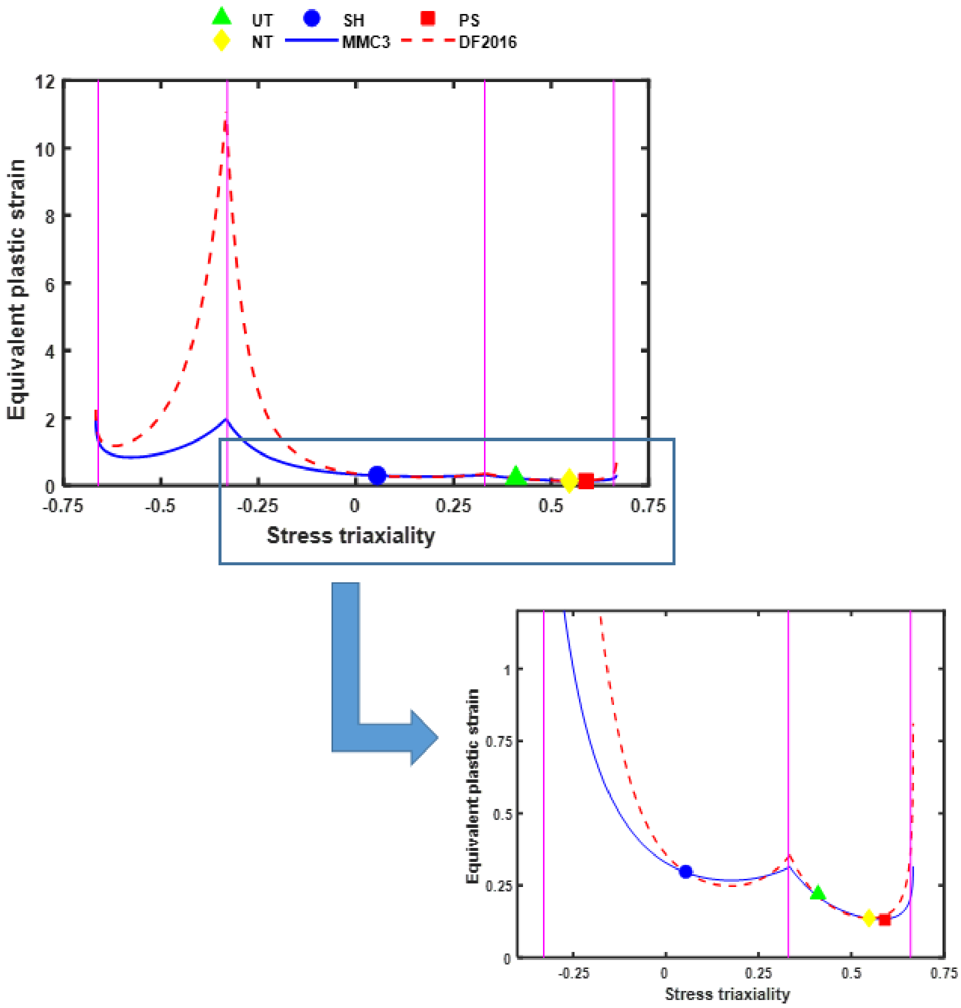

Figure 10. Comparison of the DF2016 and MMC3 fracture envelopes under plane stress, together with the corresponding calibration points

It is noteworthy that the MMC3 criterion involves three material constants for calibration.

Therefore, this criterion requires at least three fracture tests for calibration, whereas the DF2016 criterion, in addition to C, includes four additional constants (C_1 to C_4) and thus requires a minimum of four fracture tests for calibration.

Consequently, it is capable of modeling a wider range of stress states with higher accuracy.

After calibrating the criteria, tensile tests were simulated with fracture prediction using these criteria.

The results indicate that both criteria predict identical fracture locations in the specimens, which are in good agreement with experimental observations, showing only slight deviations (Figure 11).

7. Nonlinear damage accumulation

Damage in sheet metal forming processes is usually evaluated using models that account for the material's response under various loading conditions. For proportional loading, where the stress state remains constant during deformation, damage can be calculated using Eq. 20.

$$D = \int_0^{\bar{\varepsilon}^p} \frac{d\bar{\varepsilon}^p}{\bar{\varepsilon}_f^p(\eta,\mathrm{L})} \tag{20}$$

Here, D is the accumulated damage, $\bar{\varepsilon}^p$ is the equivalent plastic strain, and $\bar{\varepsilon}_f^p(\eta, L)$ is the fracture envelope, which represents the locus of equivalent plastic strains corresponding to fracture under proportional loading. This approach assumes that the stress state, defined by η and L, remains constant during deformation. Under these conditions, damage evolves uniformly, and a critical value of D=1 is generally considered to indicate fracture initiation.

In contrast, non-proportional loading involves changes in the stress state throughout deformation, making damage prediction more complex.

The evolution of η and L affects the material's damage and fracture behavior, requiring more advanced integration techniques and accurate tracking of the stress-strain history.

10.57647/jsm.2026.1801.02

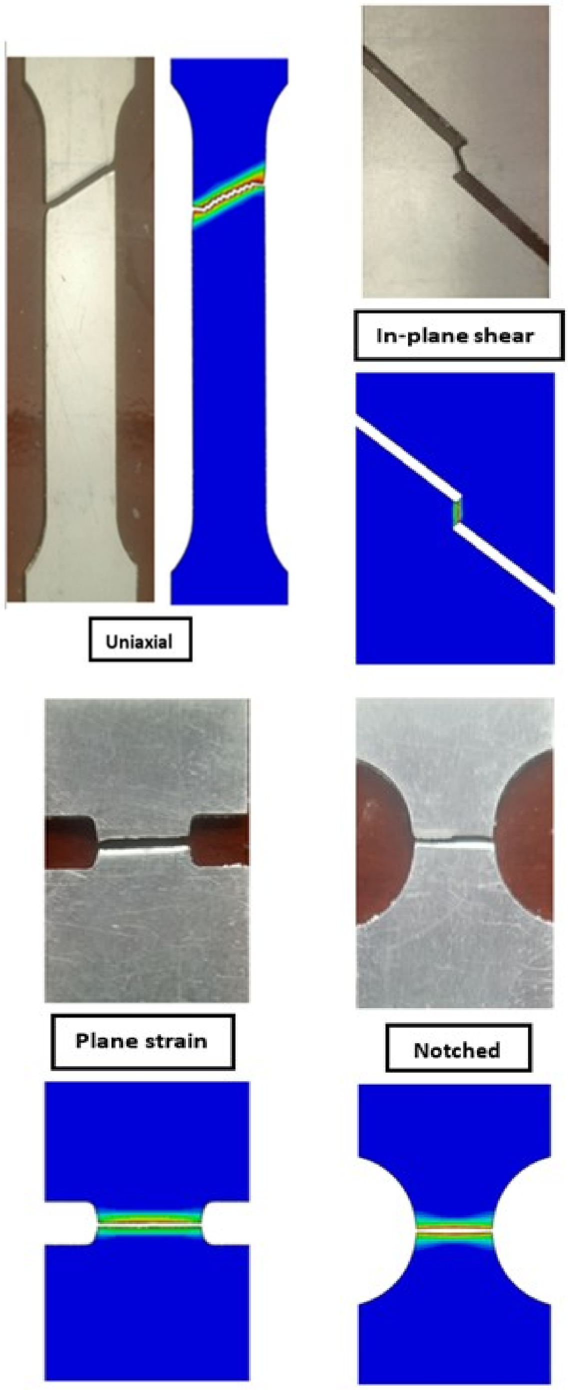

Figure 11. Fracture images of experimental calibration test specimens along with the predicted results from simulations

Due to the non-proportional loading in the SPIF process [13], the nonlinear damage accumulation rule (Eq. 21) was employed to predict fracture.

$$D = \int_0^{\bar{\varepsilon}^p} m \left(\frac{\bar{\varepsilon}^p}{\bar{\varepsilon}_f^p(\eta,\mathrm{L})} \right)^{m-1} \frac{d\bar{\varepsilon}^p}{\bar{\varepsilon}_f^p(\eta,\mathrm{L})} \tag{21}$$

To determine the parameter m in this rule, the straight groove specimen was used because of its simplicity and shorter computation time. The value of m was obtained by matching the simulated and experimental fracture depths of the straight groove specimen through iterative simulations. Forming was carried out up to a depth of 8 mm, and experimental fracture was observed at depths of 7-8 mm at both corners of the groove (Figure 12).

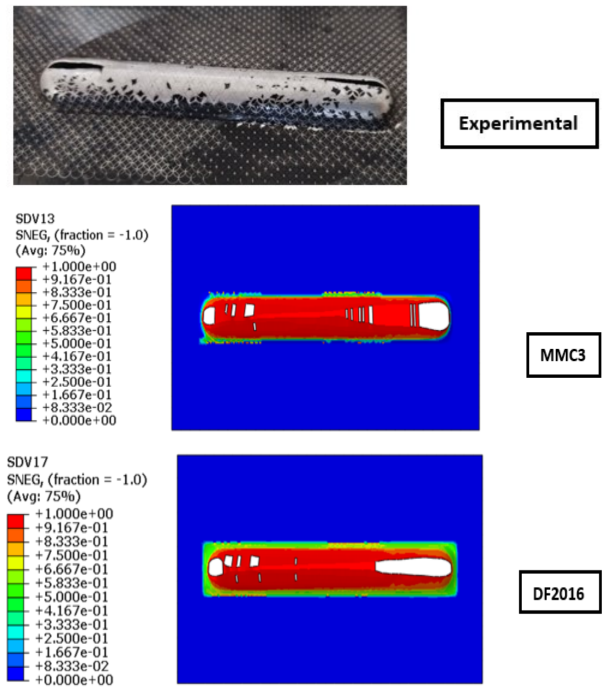

Figure 12. Fracture in the straight groove specimen with damage index simulation

The tool path in depth was zigzag shaped with a vertical pitch of 1 mm. The calibrated values of m for the two criteria are listed in Table 5. The small differences between m values indicate a nearly identical rate of damage accumulation across the two criteria. Therefore, the simulation results of these two criteria are expected to be close to each other.

Table 5. Obtained (m) values for the two criteria

criterion	m
MMC3	0.106
DF2016	0.104

8. Results and discussion

8.1. Evaluation of numerical models

To evaluate the numerical models, the thickness and in-plane strain distributions of the formed specimens were obtained both experimentally and numerically and then compared. In the experiments, the major and minor strains were determined by measuring the major and minor axes of the deformed circles marked on the specimen surfaces. The negligible minor strain compared to the major strain confirmed a plane strain deformation on the walls of the pyramidal and conical parts. For thickness measurement, the specimens were cut, and the thickness at various points was measured with a micrometer. Since the sheet is firmly clamped by the sheet holder, no material flow occurs from the clamped area to the deformation zone, causing earlier thinning. The minimum wall thickness, where cracks appeared, was observed near the bottom of the part. The experimentally obtained thickness and strain distributions were compared with the simulation results (Figure 13). The good agreement confirms the validity of the Abaqus model.

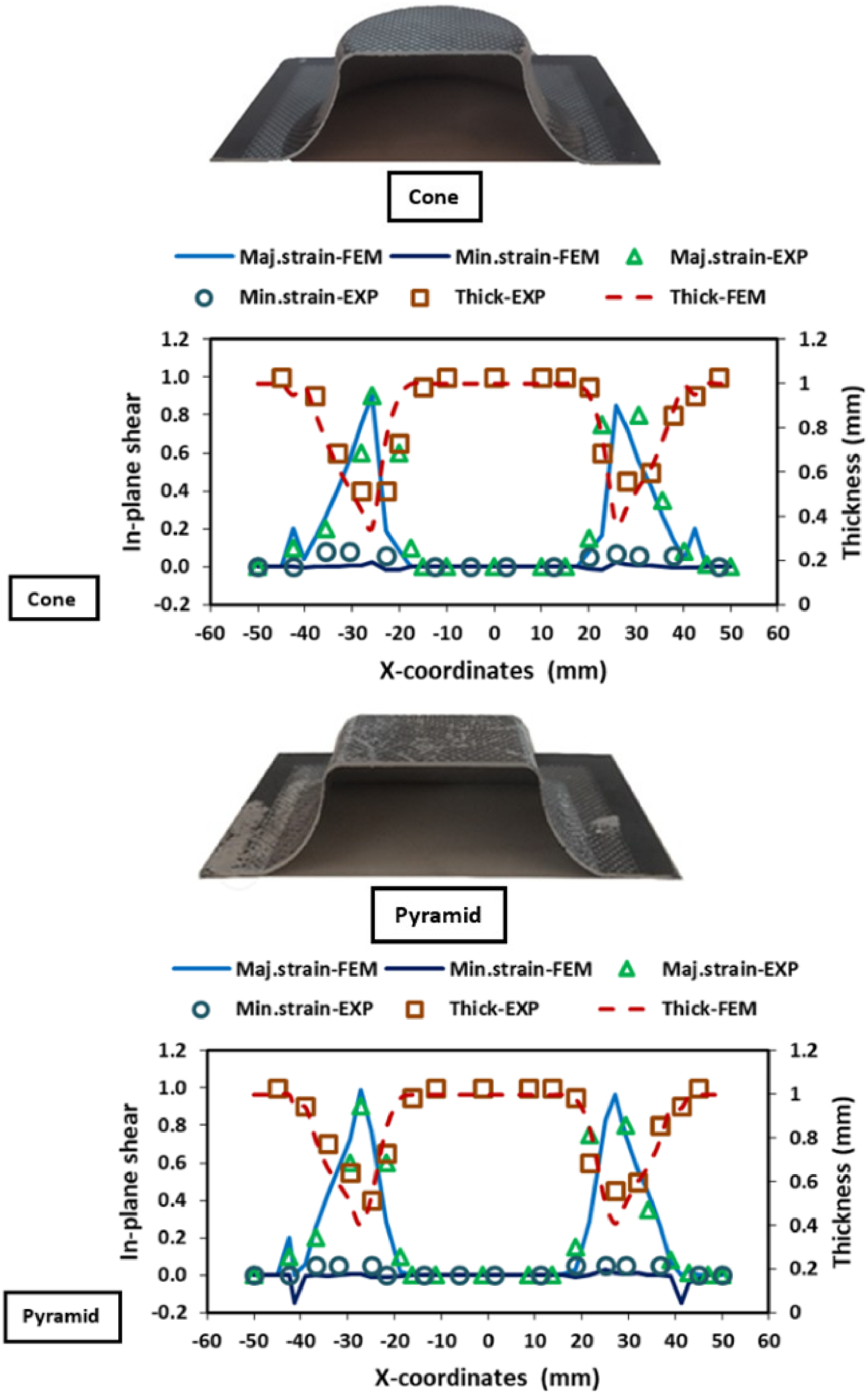

Figure 13. Cross-sectioned specimens, showing the corresponding in-plane strain and thickness distributions

8.2. Analysis of stress and strain states in SPIF

Understanding the stress and strain states in incremental forming is essential, as it not only reveals the loading characteristics and deformation mechanisms of the process but also provides a basis for selecting an appropriate damage accumulation rule for fracture analysis. To achieve this, a straight groove specimen was formed to a depth of 8 mm, and the corresponding simulation data were used to analyze the stress and strain fields. A specific element at the midpoint of the groove was selected to examine the evolution of stress and strain in detail.

As shown in Figure 14, the variation of stress triaxiality with equivalent plastic strain was investigated for both the top and bottom surfaces of this element. The results exhibit a strongly nonlinear behavior, underscoring the complexity of damage accumulation in incremental forming. Similarly, the evolution of in-plane principal strains for the same element was obtained to investigate the strain state, as shown in Figure 15.

This analysis reveals a plane strain deformation state, where the material stretches along the major strain direction without significant lateral deformation. The pronounced nonlinearity evident in both the stress triaxiality history and the strain path demonstrates that a nonlinear damage accumulation rule is not merely beneficial but indispensable for reliably predicting damage growth throughout the SPIF process. These findings confirm that SPIF involves strongly nonlinear loading paths, an essential consideration for accurate fracture prediction.

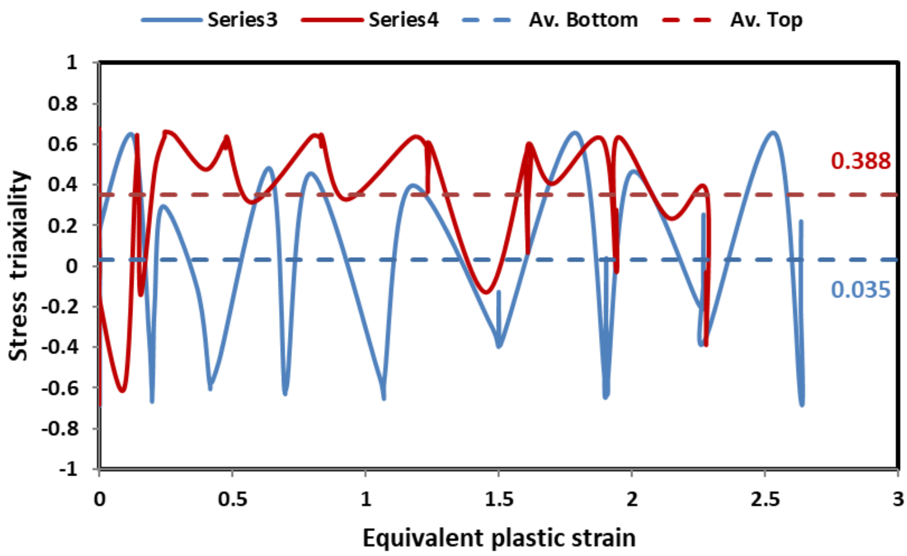

Figure 14. The variation of η with increasing $\bar{\varepsilon}^p$ for the top and bottom surfaces of the selected element

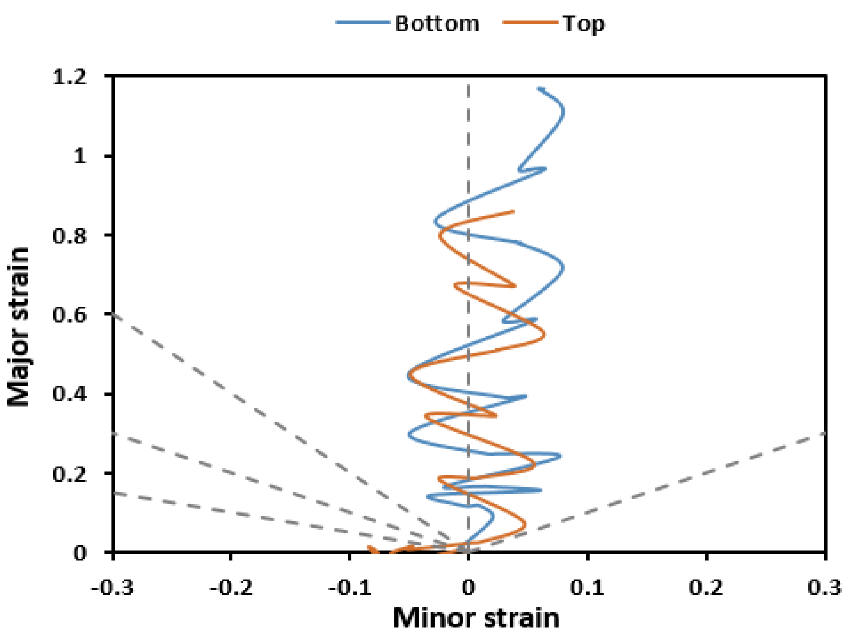

Figure 15. Strain path for the top and bottom surfaces of the selected element at the midpoint of the straight groove tool path

10.57647/jsm.2026.1801.02

The non-proportional loading nature of SPIF makes it necessary to use the nonlinear damage accumulation rule in the simulations. Following the work of Xue [23] and Mirnia [12], who demonstrated the effectiveness of this rule, Eq. 21 was implemented in Abaqus via the VUSDFLD subroutine. Figure 16 shows the linear and nonlinear damage evolution for the MMC3 and DF2016 criteria as a function of the equivalent plastic strain in an element at the middle of the straight groove path. The linear damage rule (Eq. 20) yields an almost constant slope and predicts fracture prematurely at a lower plastic strain, whereas the nonlinear rule exhibits a variable slope and predicts significantly higher fracture strains. Nonlinear damage evolution for both criteria is similar, with slightly higher rates for MMC3. Thus, DF2016 allows for larger plastic strain before fracture, implying that fracture is expected at greater depth in simulations using DF2016.

8.3. Fracture prediction in SPIF

The formed truncated conical and pyramidal specimens had a wall angle of 84.3° at a depth of 30 mm (Figure 3). Experimental fractures occurred at depths of 23-24 mm for both shapes. After calibrating the nonlinear accumulation damage rule with the groove specimen, fracture simulations were performed for the conical and pyramidal parts. The predicted crack depths and locations were compared with experimental results (Figures 17 and 18).

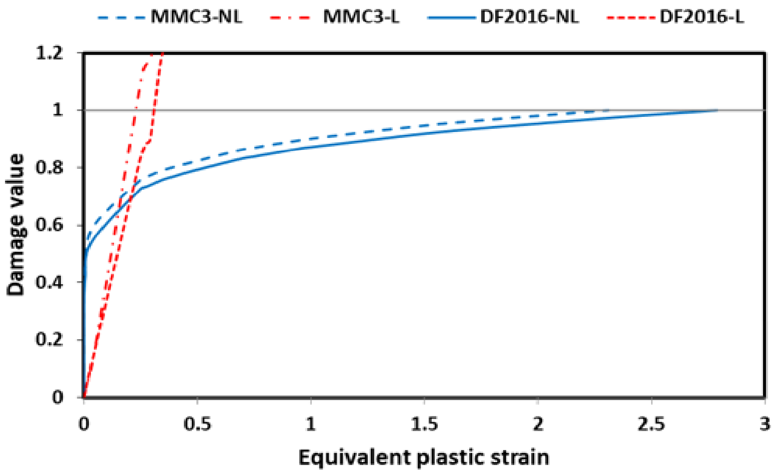

Figure 16. Damage evolution with increasing equivalent plastic strain for linear and nonlinear accumulation rules

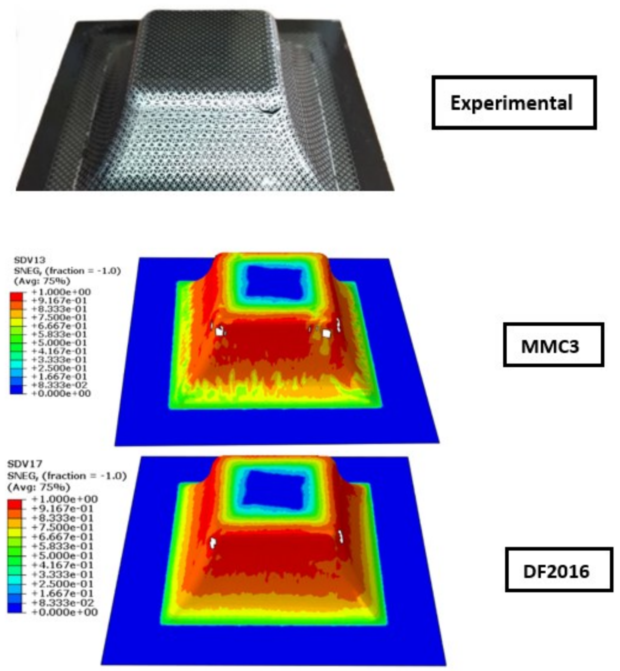

Figure 17. Fracture in the pyramidal specimen with variable wall angle along with the damage index

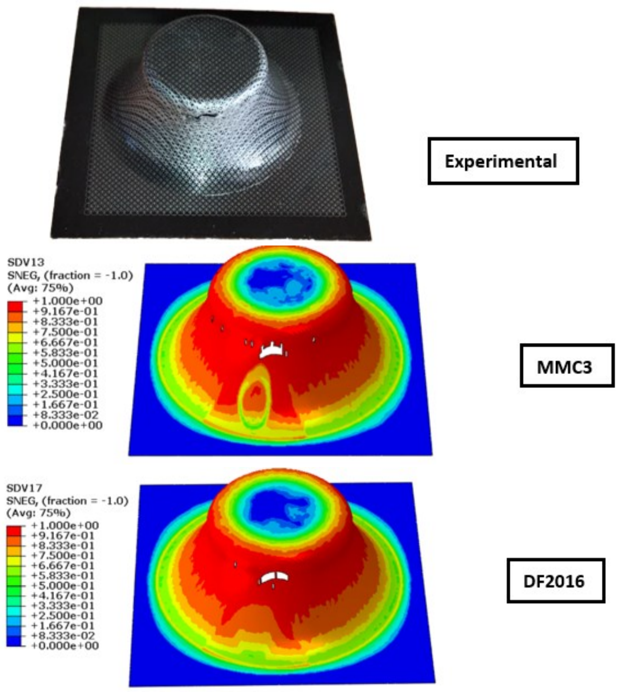

Figure 18. Fracture in the conical specimen with variable wall angle along with the damage index

10.57647/jsm.2026.1801.02

In the pyramidal specimen with a variable wall angle, fractures appeared experimentally at two opposite corners, whereas the simulations predicted cracks at all four corners for both MMC3 and DF2016.

For the conical specimen, the experimental crack appeared on one side, while the MMC3 model predicted cracks on both sides.

The DF2016 model correctly predicted a single crack, demonstrating higher accuracy.

The predicted crack depths for the truncated conical and pyramidal parts are summarized in Table 6.

Fracture in the truncated conical specimen occurs along the wall under plane-strain conditions, whereas in the pyramidal specimen it initiates at the edges under biaxial tension.

The higher stress triaxiality associated with biaxial tension accelerates void growth, leading to earlier fracture at smaller depths in the pyramid.

However, shear-driven coalescence associated with maximum shear stress in the cone wall [30], limits strain accumulation, thereby reducing the forming depth at fracture initiation.

Although the exponent m values for both criteria show negligible variation (Table 5), the damage plastic strain curves in Figure 16 indicate that MMC3 predicts crack initiation at smaller depths than DF2016 due to its higher damage rate, which is consistent with the observed results.

Overall, DF2016 provides more accurate predictions of fracture depth than MMC3.

This improved performance is attributed to the availability of four material constants in DF2016, which allows for a more flexible and accurate representation of a wider range of loading conditions compared with MMC3, which employs only three constants, leading to more precise modeling of deformation behavior in sheet metal forming processes.

Table 6. Experimentally and numerically predicted fracture depths in SPIF tests

Experiment type	criterion	Truncated cone	Truncated pyramid
FEM (mm)	MMC3	21.94	22.82
	DF2016	23.98	24.26
Exp. (mm)		23.1	23.8
Error (%)	MMC3	5.02	4.11
	DF2016	3.8	1.9

Figure 19 shows the in-plane strain distribution with damage index of all sheet elements one frame before fracture for both the truncated cone and pyramid geometries with variable wall angles. During SPIF, the tool path induces material deformation in both meridional and circumferential directions, causing meridional and circumferential tensile stresses.

The elements with zero major and minor strains represent the undeformed material in the region constrained by the clamping plate and in some regions of the bottom of the part.

Analysis of the diagram shows that the strain distribution of the elements in the conical part corresponds to a plane strain tension condition.

Moreover, the strain obtained from the MMC3 criterion is smaller than that from the DF2016 criterion, and it is therefore expected that the crack would be predicted at a smaller depth using MMC3 criterion, which is consistent with the crack depth values measured by the criteria.

The strain distribution of the elements in the pyramidal part indicates that, similar to the conical specimen, the wall regions of the pyramid experience a plane strain deformation state.

The strain state of some elements lies between plane strain tension and biaxial tension. In fact, biaxial tension occurs along the pyramid edges, where the tool changes direction.

Under biaxial tension, the material is stretched in both major and minor directions, leading to severe thinning of the sheet, which is confirmed by the presence of cracks in this region.

The fact that the strain distributions extend beyond the FFLD curves is due to the nature of the FFLD diagram, which is applicable to tests under proportional loading, whereas loading in the incremental forming process is highly non-proportional and localized.

8.4. Discussion on the cutoff value for the stress triaxiality

The cutoff values for the stress triaxiality of the DF2016 and MMC3 criteria, together with the plane stress conditions, are shown in Figure 20.

As can be seen, the MMC3 criterion predicts a significantly lower cutoff value compared to the $\sigma_1 = 0$ condition.

The DF2016 criterion also indicates a lower value than $\sigma_1 = 0$ as a function of the Lode parameter.

These lower cutoff values, compared with the $\sigma_1 = 0$ condition, demonstrate that both criteria are capable of capturing compressive dominated stress states and tensile loading states that occur during the forming process.

Given that the stress states are predominantly characterized by plane-strain tension and biaxial tension, both criteria are expected to effectively capture the diverse loading conditions inherent in the incremental forming process and accurately predict the resulting stress states.

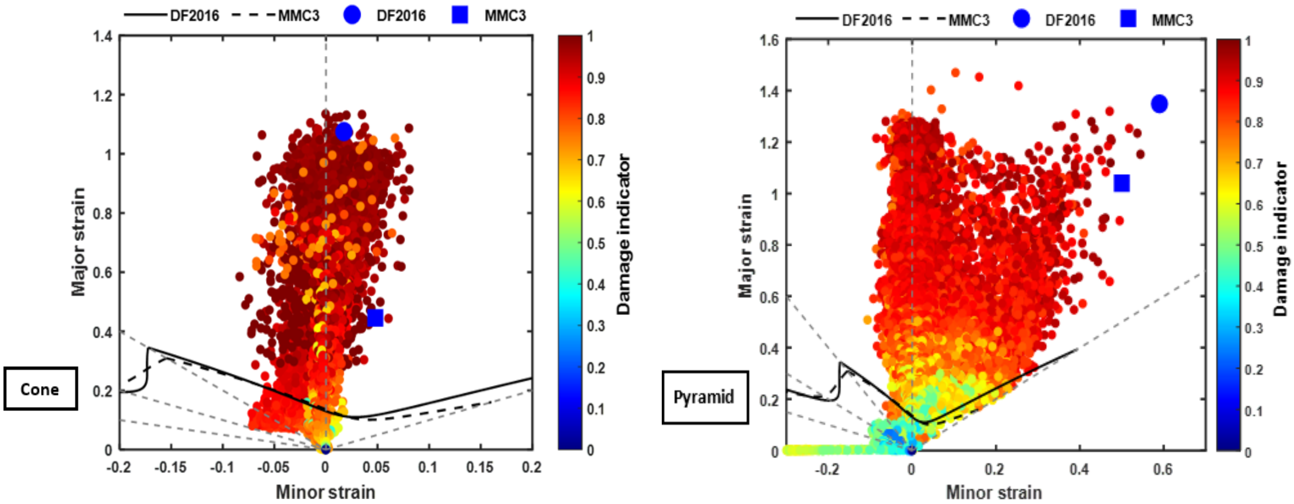

Figure 19. In-plane strain distribution of all sheet elements in one frame before the onset of fracture

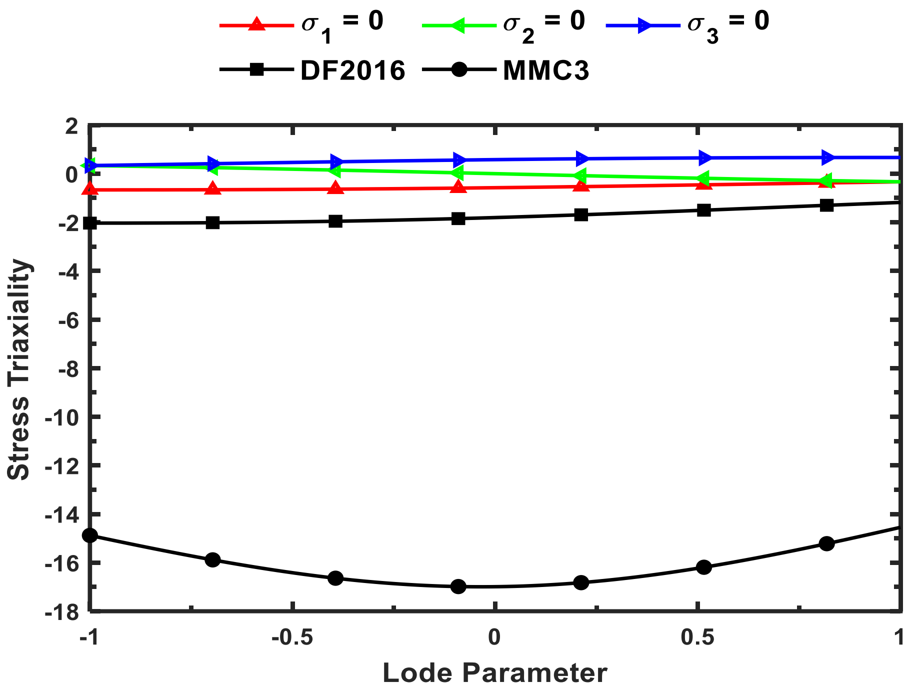

Figure 20. The cutoff planes of the DF2016 and MMC3 criteria along with the plane stress conditions

9. Conclusion

This study investigated the predictive capabilities of the MMC3 and DF2016 fracture criteria for determining the depth and location of crack initiation in truncated pyramidal and conical specimens with variable wall angle formed by single point incremental forming (SPIF) of a 1 mm thick AA1050 aluminum alloy sheet. Finite element simulations conducted in Abaqus/Explicit 2022 were validated against experimental data. The main conclusions are summarized as follows:

- While both the MMC3 and DF2016 criteria yielded acceptable predictions for crack depth and location in both geometries, the DF2016 criterion demonstrated superior overall accuracy and reliability.
- The enhanced performance of DF2016 is attributed to its formulation, which incorporates a greater number of material constants and models the cutoff value for the stress triaxiality as a function of the Lode parameter. This allows DF2016 to capture a wider range of deformation modes with higher precision, leading to more accurate fracture predictions.
- Although both criteria exhibited similar damage evolution rates, the marginally higher rate predicted by MMC3 results in a slightly smaller fracture depth, a trend that was confirmed by the simulation results.
- The strain state along the wall of the conical specimen is characterized by plane strain tension, with the major strain oriented meridionally and the minor strain near zero in the circumferential direction. This strain state

promotes circumferential crack initiation near the region of maximum thinning at the part bottom.

- While biaxial tension in the pyramidal part edge leads to higher stress triaxiality and void growth, factors that typically promote earlier fracture, the shear-controlled void coalescence mechanism, driven by higher maximum shear stress in the truncated cone, accelerates damage evolution in the conical part. This results in fracture at lower strains and a smaller forming depth for the conical geometry compared to the pyramidal one.
- The cutoff values for stress triaxiality predicted by both DF2016 and MMC3 are lower than those corresponding to the $\sigma_1 = 0$ condition, confirming their capability to capture both compressive and tensile stress states present in SPIF. Furthermore, the observed stress triaxiality range of $-\frac{2}{3} \leq \eta \leq \frac{2}{3}$ in both geometries demonstrates that both criteria are well-suited for modeling the principal loading conditions in incremental forming.

Authors Contribution
All the authors have participated sufficiently in the intellectual content, conception and design of this work or the analysis and interpretation of the data (when applicable), as well as the writing of the manuscript.

Availability of data and materials
The data that support the findings of this study are available from the corresponding author, upon reasonable request.

Conflict of interests
The author states that there is no conflict of interest.

References

[1] Patel D, Gandhi A. A review article on process parameters affecting Incremental Sheet Forming (ISF). Mater Today Proc. 2022;63:368-75. doi: https://doi.org/10.1016/j.matpr.2022.03.208

[2] Skjoedt M. Rapid prototyping by single point incremental forming of sheet metal [dissertation]. Lyngby: Technical University of Denmark; 2008. Available from: https://orbit.dtu.dk/en/publications/rapid-prototyping-by-single-point-incremental-forming-of-sheet-me

[3] Cheng Z, Li Y, Xu C, Liu Y, Ghafoor S, Li F. Incremental sheet forming towards biomedical implants: A review. J Mater Res Technol. 2020;9(4):7225-51. doi: https://doi.org/10.1016/j.jmrt.2020.04.096

[4] Jeswiet J, Micari F, Hirt G, Bramley A, Duflou J, Allwood J. Asymmetric single point incremental forming of sheet metal. CIRP Ann. 2005;54(2):88-114. doi: https://doi.org/10.1016/S0007-8506(07)60021-3

[5] Reddy NV, Lingam R, Cao J. Incremental metal forming processes in manufacturing. In: Handbook of manufacturing engineering and technology. Springer; 2015. p. 411-52.

[6] Pineau A, Benzerga AA, Pardoen T. Failure of metals I: Brittle and ductile fracture. Acta Mater. 2016;107:424-83. doi: https://doi.org/10.1016/j.actamat.2015.12.034

[7] Emmens W, van den Boogaard AH. An overview of stabilizing deformation mechanisms in incremental sheet forming. J Mater Process Technol. 2009;209(8):3688-95. doi: https://doi.org/10.1016/j.jmatprotec.2008.10.003

[8] Jackson K, Allwood J. The mechanics of incremental sheet forming. J Mater Process Technol. 2009;209(3):1158-74. doi: https://doi.org/10.1016/j.jmatprotec.2008.03.025

[9] Talesh RBM, Keshtiban PM, Oskui AE. Investigation of mode-I fracture behavior by essential work of fracture during the single-point incremental forming process. Eng Fail Anal. 2023;154:107677. doi: https://doi.org/10.1016/j.engfailanal.2023.107677

[10] Sharma M, Bhattacharya A, Paul SK. Failure behavior in single point incremental forming parts of AA6061-T6. Eng Fail Anal. 2025;149:109682. doi: https://doi.org/10.1016/j.engfailanal.2025.109682

[11] Kumar A, Mehtani H, Shrivastava A, Mishra S, Narasimhan K, Samajdar I. Failure mechanism during incremental sheet forming of a commercial purity aluminum alloy. Eng Fail Anal. 2023;146:107090. doi: https://doi.org/10.1016/j.engfailanal.2023.107090

[12] Gatea S, Ou H, Lu B, McCartney G. Modelling of ductile fracture in single point incremental forming using a modified GTN model. Eng Fract Mech. 2017;186:59-79. doi: https://doi.org/10.1016/j.engfracmech.2017.09.021

[13] Mirnia MJ, Shamsari M. Numerical prediction of failure in single point incremental forming using a phenomenological ductile fracture criterion. J Mater Process Technol. 2017;244:17-43. doi: https://doi.org/10.1016/j.jmatprotec.2017.01.029

[14] Wang C, Daniel WJ, Lu H, Liu S, Meehan PA. A comparative investigation of damage models for fracture prediction in two-point incremental forming. Int J Adv Manuf Technol. 2021;112:3069-81. doi: https://doi.org/10.1007/s00170-020-06587-x

[15] Bharti S, Gupta A, Krishnaswamy H, Panigrahi S, Lee MG. Evaluation of uncoupled ductile damage models for fracture prediction in incremental sheet metal forming. CIRP J Manuf Sci Technol. 2022;37:499-517. doi: https://doi.org/10.1016/j.cirpj.2022.02.023

[16] Kumar P, Tandon P. Investigating the capability of the Lemaitre damage model to establish the incremental sheet forming process. Arch Civ Mech Eng. 2022;22(2):66. doi: https://doi.org/10.1007/s43452-022-00391-y

[17] Kasaei MM, Pereira JA, Carbas RJ, Marques EA, da Silva LF. Ductile fracture prediction in hole hemming of aluminum and magnesium sheets. Metals. 2023;13(9):1559. doi: https://doi.org/10.3390/met13091559

[18] Lou Y, Huh H, Lim S, Pack K. New ductile fracture criterion for prediction of fracture forming limit diagrams of sheet metals. Int J Solids Struct. 2012;49(25):3605-3615. doi: https://doi.org/10.1016/j.ijsolstr.2012.02.016

[19] Lou Y, Huh H. Extension of a shear-controlled ductile fracture model considering the stress triaxiality and the Lode parameter. Int J Solids Struct. 2013;50(2):447-455. doi: https://doi.org/10.1016/j.ijsolstr.2012.10.007

[20] Lou Y, Yoon JW, Huh H. Modeling of shear ductile fracture considering a changeable cut-off value for stress triaxiality. Int J Plast. 2014;54:56-80. doi: https://doi.org/10.1016/j.ijplas.2013.08.006

[21] Lou Y, Chen L, Clausmeyer T, Tekkaya AE, Yoon JW. Modeling of ductile fracture from shear to balanced biaxial tension for sheet metals. Int J Solids Struct. 2017;112:169-184. doi: https://doi.org/10.1016/j.ijsolstr.2016.11.034

[22] Behrens B, Rosenbusch D, Wester H, Althaus P. Comparison of three different ductile damage models for deep drawing simulation of high-strength steels. In: IOP Conference Series: Materials Science and Engineering. Vol 1238. Bristol, UK: IOP Publishing; 2022. p. 012021. doi: https://doi.org/10.1088/1757-899X/1238/1/012021

[23] Wang S, Wang Y, Yu L, Ji K, Liu X, Lou Y. Failure Modeling for QP980 Steel by a Shear Ductile Fracture Criterion. Metals. 2022;12(3):452. doi: https://doi.org/10.3390/met12030452

[24] Zeinali MS, Naeini HM, Talebi-Ghadikolaee H, Panahizadeh V. Numerical and experimental investigation of fracture in roll forming process using Lou–Huh fracture criterion. Arabian Journal for Science and Engineering. 2022;47(12):15591-15602. doi: https://doi.org/10.1007/s13369-022-06662-3

[25] Akşen TA, Özsoy N, Esener E, Özsoy M, Fırat M. Predicting the fracture initiation of dual-phase steels under different stress paths through an implicit stress update scheme. Eng Fail Anal. 2025;175:109578. doi: https://doi.org/10.1016/j.engfailanal.2025.109578

[26] Nielsen CV, Martins PA. Metal forming: formability, simulation, and tool design. Cambridge, MA: Academic Press; 2021.

[27] Bai Y, Wierzbicki T. Application of extended Mohr–Coulomb criterion to ductile fracture. Int J Fract. 2010;161(1):1-20. doi: https://doi.org/10.1007/s10704-009-9422-8

[28] Mahmoodi M, Tagimalek H, Maraki M, Karimi S. Experimental and numerical investigation of the formability of cross and accumulative roll bonded 1050 aluminum alloy sheets in single point incremental forming process. Int J Eng. 2022;35:1707-1715.

[29] Tayebi P, Hashemi R. Study of single point incremental forming limits of Al 1050/Mg-AZ31B two-layer sheets fabricated by roll bonding technique: Finite element simulation and experiment. J Mater Res Technol. 2024;29:149-169.

[30] Gatea SM. Experimental and numerical investigation of formability and ductile fracture in incremental sheet forming. [dissertation]. Nottingham, UK: University of Nottingham; 2017.